Journal of Materials Chemistry A

ROYAL SOCIETY OF CHEMISTRY

PAPER

View Article Online
View Journal | View Issue

Check for updates

Cite this: J. Mater. Chem. A, 2022, 10, 24938

Mixed-metal Zr/Ti MIL-173 porphyrinic metal–organic frameworks as efficient photocatalysts towards solar-driven overall water splitting†

Ben Gikonyo,[a] Eva Montero-Lanzuela,[b] Herme G. Baldovi,[b] Siddhartha De,[a] Catherine Journet,[a] Thomas Devic,[c] Nathalie Guillou,[d] Davide Tiana,[e] Sergio Navalon*[b] and Alexandra Fateeva*[a]

Received 22nd August 2022
Accepted 9th November 2022

DOI: 10.1039/d2ta06652a

rsc.li/materials-a

Hydrolytically stable MOFs combining Ti(IV) ions and porphyrin ligands are expected to display outstanding photophysical properties, making them ideal photocatalysts for the overall water splitting reaction under solar light. We report here the one-pot synthesis of a microporous MOF built up from a phenolate-based porphyrin ligand and a mixture of Zr(IV) and Ti(IV) ions. A broad set of characterization tools (PXRD, SEM-EDX, TEM, STEM-EDX, solid state UV-vis spectroscopy, XPS, nitrogen sorption) along with DFT calculations were used to confirm that Ti(IV) ions are uniformly inserted in the MIL-173 structure and located in the inorganic building unit. MIL-173(Zr/Ti)-40, containing 40 at% of Ti(IV), exhibits exceptional photocatalytic activity for the overall water splitting into H_2 and O_2 under simulated sunlight irradiation, without the use of any co-catalyst or sacrificial agent. This material operates efficiently under a photoinduced charge separation mechanism as revealed by photocurrent measurements and photoluminescence spectroscopy. This study provides insights for the development of efficient MOF-based materials as photocatalysts for the solar-driven overall water splitting.

Introduction

Chemical synthesis of metal–organic frameworks (MOFs) allows us to combine properties of the linker molecules and the metal ions, and even to achieve synergetic effects through the interaction of both organic and inorganic building units.[1] In the last few years MOF-based materials have been envisioned as efficient emerging heterogeneous photocatalysts for the production of solar fuels.[2–4] Of particular interest in the field has been the use of MOFs as heterogeneous photocatalysts for the generation of H_2 from water. In 2010 García and co-workers reported for the first time the possibility of using MOFs such as UiO-66(Zr)–X (X: H or NH_2) as photocatalysts for the hydrogen evolution reaction (HER) from water using methanol as the sacrificial electron donor and UV-vis irradiation.[5] Since then, the number of studies using MOFs for the solar-driven HER increased significantly, reflecting the interest in the field.[6–9] From the point of view of application, however, it would be desirable to develop MOF-based materials as photocatalysts to promote the overall water splitting (OWS) under sunlight irradiation into H_2 and O_2 in the absence of sacrificial electron donors or noble metals.[10,11] In 2017, Huang, Liu and co-workers reported a seminal work using MIL-53(Al)–NH_2 in the presence of Ni(II) cations coordinated to the amino group of the terephthalate ligand as a co-catalyst to promote the photocatalytic OWS under UV-vis light irradiation.[12] Later, a series of theoretical[13,14] and experimental studies have shown the potential use of MOFs and MOF composites based on UiO-66,[15,16] MIL-125,[17–19] among others[20–22] for the photocatalytic OWS. Regardless of the good achievements made during the first five years, the field is still in its infancy. In fact, most of the MOF-based materials employed for this purpose exhibit relatively low visible light absorption (below 450 nm)[15] or have employed noble metal-based co-catalysts[18,22] such as Pt, Ru or Ir, which present inherent problems of limited availability and low stability, to improve the photocatalytic activity.

In this context, combining a photosensitizer with a semiconductor is a classical approach to enhance the performance aiming for a broad and efficient light absorption as well as promoting charge separation.[23] Along with photophysical properties, chemical stability is of paramount importance for material applications. For example, for OWS, a high stability in

[a]Laboratoire des Multimatériaux et Interfaces, Université Lyon, Université Claude Bernard Lyon 1, UMR CNRS 5615, F-69622 Villeurbanne, France. E-mail: alexandra.fateeva@univ-lyon1.fr

[b]Departamento de Química, Universitat Politècnica de València, C/Camino de Vera, s/n, 46022 Valencia, Spain

[c]Nantes Université, CNRS, Institut des Matériaux de Nantes Jean Rouxel, IMN, F-44000 Nantes, France

[d]Institut Lavoisier de Versailles, UMR 8180 CNRS UVSQ, Université Paris-Saclay, 45 Avenue des Etats-Unis, 78035 Versailles, France

[e]School of Chemistry, University College Cork, College Rd, Cork, Ireland

† Electronic supplementary information (ESI) available. See DOI: https://doi.org/10.1039/d2ta06652a

water is mandatory. It is well established now that the combination of high valence (+3 and +4) cations and hard donor oxygen coordinating groups leads to hydrolytically stable MOFs.[24] On top of that, some of the hydrolytically stable Ti(IV) MOFs have drawn great attention for photocatalytic applications.[25,26] Especially, the combination of Ti-oxo units with visible light absorbing ligands brought important progress with development of benchmark compounds such as the MIL-125(Ti)–NH_2 [23,27,28] based on Ti and aminoterephthalate. Porphyrins on the other side are natural light harvesters, and have been used to build photoactive MOFs given their high absorption in the visible region.[29,30] Porphyrin-based MOFs are among the most appropriate photocatalysts reported for the solar-driven HER due to their efficient visible light absorption.[31] As far as we know, only two titanium and porphyrin based crystalline MOFs have been reported for now: PCN-22 built from the tetracarboxylate TCPP and Ti_7O_6 oxo-cluster,[32] and DGIST-1 based on the same linker and Ti-oxo chain.[33] Both compounds displayed photocatalytic activity for benzyl alcohol oxidation. Generally, the synthesis of crystalline and porous Ti-based coordination polymers is challenging due to the high reactivity of Ti^{4+} and the easy hydrolysis of Ti precursors.[26] An alternative strategy is to incorporate titanium into more widely available Zr-based MOFs, leading to mixed metal Zr/Ti frameworks, providing semiconductor-like Ti-oxo clusters combined with a broader range of ligands. It is noteworthy that a few theoretical[13,14] and experimental[15] reports dealing with UiO-66 solids pointed out the possibility to increase the efficiency of these materials for OWS through the preparation of multimetallic analogs with Zr, Ce or Ti ions in the metal nodes. This favors the photoinduced ligand-to-metal charge transfer mechanism even under visible light irradiation. Two main strategies are employed to obtain mixed metal Zr/Ti UiO-66 type frameworks: either a Post Synthesis Metal Exchange (PSME) or a one-pot Ti incorporation during the MOF synthesis. The former approach is far more extensively studied since the first report by Cohen *et al.* in 2012.[34] PSME in UiO-66(Zr)[15,35–37] and its analogues (UiO-66(Zr)–NH_2)[38–41] has been reported using various Ti precursors and exchange conditions (solvothermal, microwave). However, the PSME strategy was deeply questioned in 2018 by the report of Cohen *et al.*, who used Transmission Electron Microscopy (TEM) of Ti exchanged UiO-66 samples to reveal a surface deposition of nanoscale titanium oxide giving rise to a MOF@TiO_2 composite rather than a mixed metal–organic framework.[42] This study relies on local rather than bulk characterization of MOF particles and suggests that most of the reports about the enhanced catalytic properties of metal exchanged UiO-66 might have to be reinterpreted. The second strategy involves Ti incorporation during the MOF synthesis and is far less reported, moreover it was never explored to date in porphyrinic MOFs. Han *et al.* used the latter approach to achieve Ti doped UiO-66 by using a mixture of zirconium chloride and titanium isopropoxide as metallic reactants during the MOF synthesis.[43] By adjusting the inorganic precursor composition, solids with a Ti content ranging from 5 to 33 at% were prepared, retaining the crystallinity, microporosity and affecting the particle size and morphology. The Ti doped MOFs displayed enhanced sorption capacity toward anionic organic dyes in comparison to the monometallic MOF. In light of the questioning about the actual Ti metathesis by PSME, the one-pot approach seems somehow less controversial. Nevertheless, preparing homogeneous bimetallic MOFs requires the concomitant reaction of both cations. This can be done by altering the nature of the metallic precursors and their very structure-dependent reaction kinetics. As an example, bimetallic MIL-53 made of very different cations (reactive Fe(III) and kinetically inert Cr(III)) was obtained by adjusting the nature of the iron and chromium precursors.[44] Still the one-pot strategy remains underexplored for Ti-containing MOFs, and no reports are available for MOFs based on phenolate coordinating groups.

With these precedents in mind, the present study reports the development of mixed-metal MIL-173(Zr/Ti) porphyrin-based MOFs with high photocatalytic activity for the OWS under simulated sunlight irradiation. The series of mixed-metal porphyrin-based MOFs were prepared by a one-pot methodology that allowed the gradual incorporation of Ti into a stable polyphenolate porphyrin-based MIL-173(Zr) framework.[45] In-depth material characterizations based on powder X-ray diffraction (PXRD), electronic microscopy, textural and spectroscopic studies combined with periodic Density Functional Theory (DFT) calculations demonstrate that Ti is inserted in the rod-like inorganic building unit. This allows a progressive tuning of the MOF properties in terms of optical response, with preserved crystallinity and porosity. The solid containing 40 at% of Ti, MIL-173(Zr/Ti)-40 presents a photocatalytic activity for the OWS under simulated sunlight irradiation that ranks this material among the most active MOFs, even in the absence of any co-catalyst. Photocurrent measurements and photoluminescence spectroscopy experimentally prove that the activity of the best performing sample is promoted by a photoinduced charge separation reaction mechanism, which is supported by the calculation of the frontier orbitals by DFT. This study contributes to the development of more efficient MOF-based photocatalysts for the solar-driven OWS.

Results and discussion

Synthesis and characterization of mixed Zr/Ti MOFs

MIL-173(Zr) was selected as a scaffold for the incorporation of Ti. This MOF is prepared from 5,10,15,20-tetrakis(3,4,5-trihydroxyphenyl)porphyrin or H_{14}TGalPP. It combines a decent microporosity ($S_{BET} \sim 920\ m^2\ g^{-1}$) and a high stability in water, even under diluted conditions.[45] Its tetragonal structure consists of chains of edge-sharing ZrO_8 polyhedra along the *c*-axis connected by partially deprotonated $H_6TGalPP^{8-}$ ligands lying in the *a*,*b*-plane (see Fig. 1a). It is noteworthy that, in contrast with carboxylate MOFs, the O atoms surrounding Zr arose exclusively from the ligand, as no oxo or hydroxo coordination occurs even if the synthesis is carried out in a water-rich solvent. This is in line with the stronger affinity of gallate for Zr(IV) when compared to carboxylate.[46,47]

Previous study demonstrated an efficient diffusion of metallic precursors inside MIL-173 pores.[45,48] Thus, mixed metal MIL-173 preparation was first tested by the PSME on MIL-

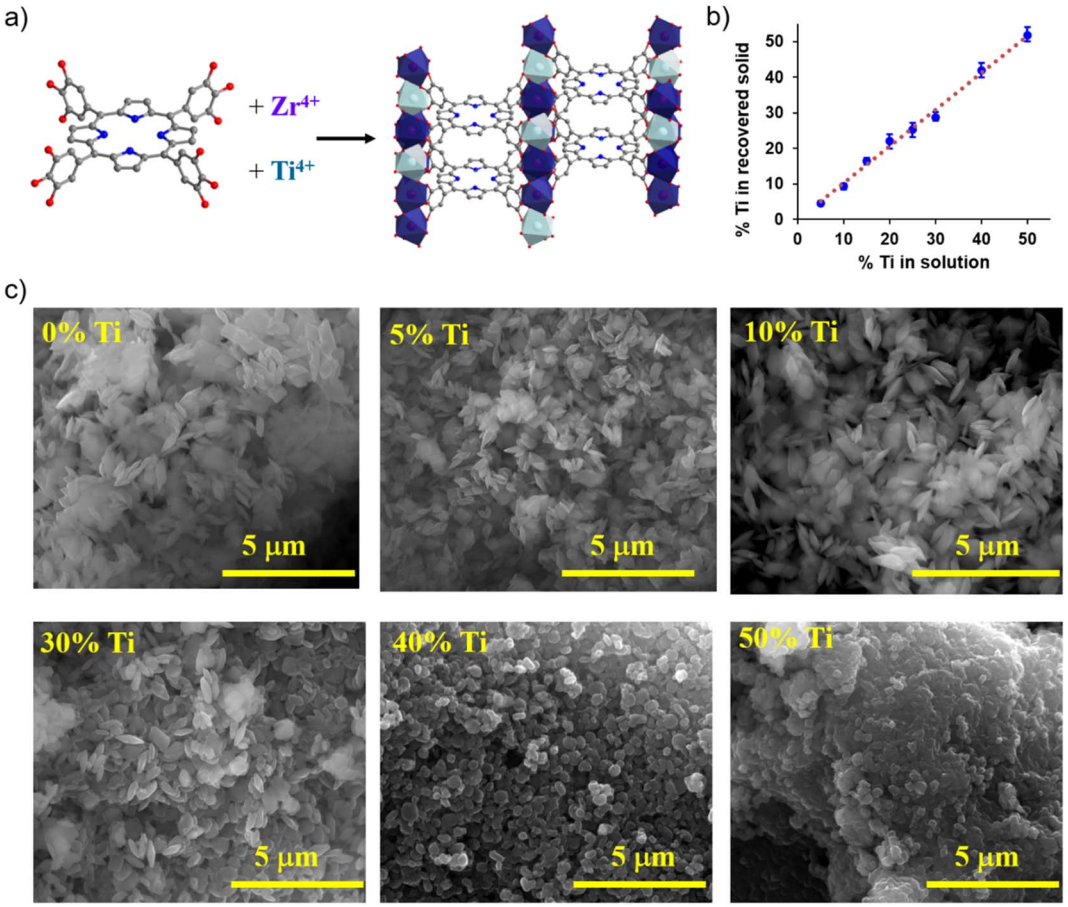

Fig. 1 Synthesis scheme for the mixed metal MIL-173(Ti/Zr) (a), Ti average content with standard deviation in the solids as obtained from EDS analysis in relation to the Ti content in the reacting solution (b). SEM images of MIL-173(Ti/Zr) samples of variable Ti content (c).

173(Zr) with Ti isopropoxide in anhydrous DMF in an inert atmosphere (see the ESI† for more information). The recovered solids were analyzed by Scanning Electron Microscopy (SEM) (Fig. S2†) and Energy Dispersive Spectroscopy (EDS). For each Ti loading tested (33 and 50 at% of Ti), the resulting material presented very high heterogeneity in terms of the Ti/Zr content in different areas of the sample, showing the limitations of the PSME in the case of MIL-173 (Table S4†). Therefore, the PSME strategy was not pursued for titanium incorporation. Much more homogeneous mixed metal MIL-173 samples were achieved by mixing a titanium precursor with zirconium chloride in the reacting solution in a chosen molar ratio. In the first trials, titanium isopropoxide was used and despite some gelation of the reacting solution, MIL-173 was formed for up to 40 at% Ti, with a good sample homogeneity for the titanium content from the SEM/EDS analysis (see Fig. S4 and Table S5†). Nevertheless, the crystallinity and the porosity of the material decreased rapidly when the content of Ti increased (Fig. S3 and S5†). The high reactivity and easy hydrolysis of titanium isopropoxide under the reaction conditions (DMF/water as the solvent) are expected to be accountable for the crystallinity and porosity loss. Therefore, a more suitable titanium precursor was sought, and synthesis attempts were made with an oxy-carboxylate complex: titanium bis-ammonium lactato dihydroxide (TiBALD). In this compound, titanium is chelated by an oxy-carboxylate ligand, which provides a stable Ti complex in aqueous solution under ambient conditions and slower reaction kinetics for ligand exchange during MOF formation. The hydrostability of TiBALD makes it particularly an attractive Ti precursor,[47,49] still in MOF chemistry its use remains underexplored. In the case of MIL-173, we performed the synthesis with variable TiBALD/$ZrCl_4$ ratios ranging from 0 to 1. Some extent of gelation was still observed during the synthesis. However, the resulting materials could be collected as crystalline powders after drying in air.

The morphology of samples was observed by SEM and the Ti/Zr content was deduced from EDS analysis. An excellent agreement between the Ti content in the reacting mixture and in the final solid was observed for all Ti/Zr ratios (Fig. 1b) suggesting that both Zr and Ti precursors react in a similar manner with the phenolate linker. MIL-173(Zr) is obtained in the shape of flattened octahedral crystals with an average size of 700 nm (Fig. 1c). Very similar crystallite size and morphology are obtained for mixed metal samples up to 30 at% Ti; from this loading the particle size decreases and the octahedron edges start to be ill-defined. For higher Ti loading, the particles become more spherical and their size continues to drop towards 400 and 200 nm for 40 and 50 at% respectively (Fig. 1c).

To gain further knowledge on the titanium distribution in a single MOF particle, TEM analysis was performed on the parent MIL-173(Zr) and the 40 at% titanium containing MIL-173(Zr/Ti)-40. The later mixed-metal sample was chosen because, as will be discussed later, it displayed the highest photocatalytic performance. The low resolution TEM micrographs obtained for the parent MIL-173(Zr) illustrate that it is composed of bipyramidal particles (Fig. 2a) that turn out to be single crystals as evidenced by the Selected Area Electron Diffraction (SAED, inset Fig. 2a) which clearly shows aligned bright spots, representative of a single crystal oriented along the *c*-axis with respect to the electron beam. High Resolution Transmission Electron Microscopy (HRTEM) performed on the edge of one particle shows the perfect atomic arrangement of the planes, spaced 1.4 nm apart, distance characteristic of the *a* parameter of the lattice (inter-chain distance of $a/2 = 14.4$ Å according to the crystal structure), in agreement with the *c*-axis orientation of the crystal (Fig. 2b). HRTEM performed on MIL-173(Zr/Ti)-40 (Fig. 2c) as well as the corresponding SAED pattern (inset Fig. 2c) confirms the crystalline nature of the titanium containing MOF. The inter-plane distance remains 1.4 nm as in the case of the parent MIL-173(Zr). STEM-EDX mapping on a single particle shows that Ti is homogeneously distributed inside the particle rather than on the particle edges, indicating coordination by the linker in the MOF structure as for Zr.

PXRD analysis revealed the formation of the crystalline MIL-173 phase for the mixed metal samples up to 50 at% Ti, although Bragg peak broadening became noticeable from 35 at% Ti (Fig. 3a). High resolution PXRD (HRPXRD) was recorded

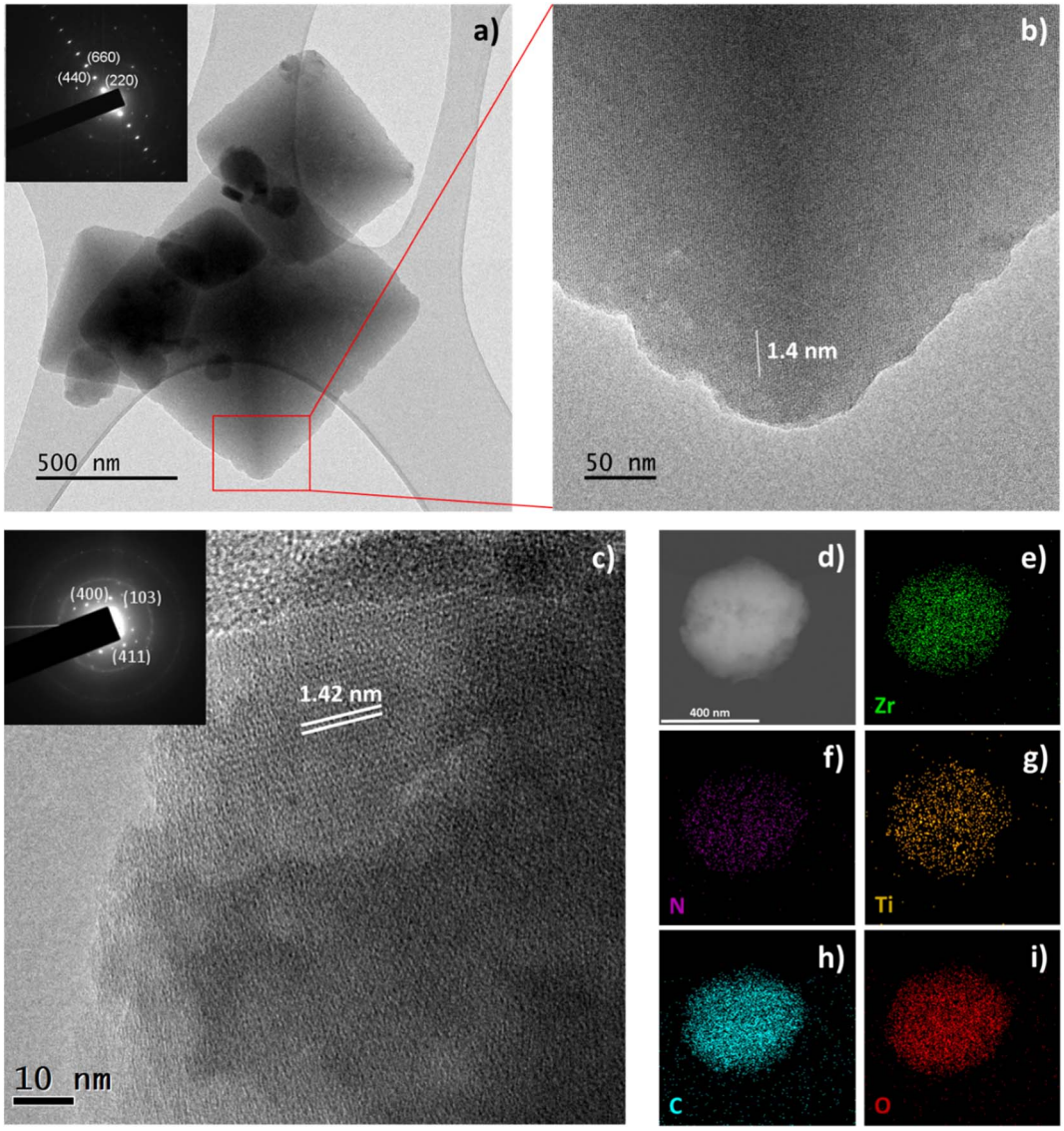

Fig. 2 TEM characterization of MIL-173. Low resolution image of MIL-173(Zr) bipyramidal single crystal particles; inset: corresponding SAED pattern (a), high resolution image performed on the edge of the particle showing the atomic arrangement of the planes (b), high resolution image of the MIL-173(Zr/Ti) crystalline particle, inset: corresponding SAED pattern (c), STEM image of MIL-173(Zr/Ti) crystalline particle (d), (e)–(i) elemental maps of (e) Zr, (f) N, (g) Ti, (h) C and (i) O respectively based on the respective Kα signals of C, N, O, Ti and the Lα of Zr in STEM-EDX.

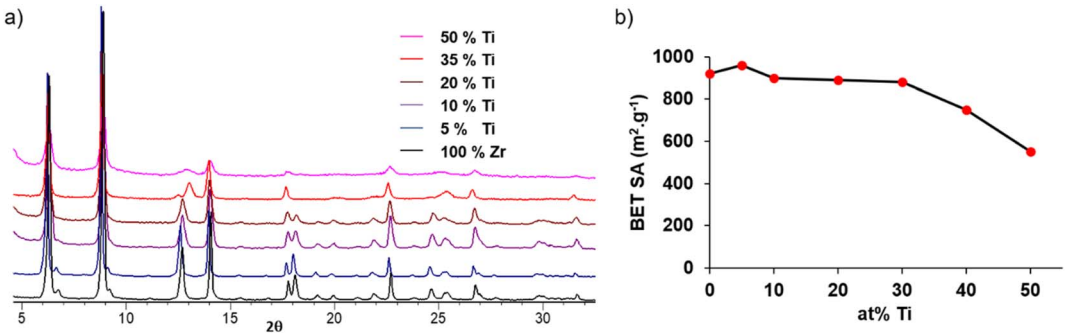

Fig. 3 MIL-173(Zr/Ti) with variable Ti content: evolution of the PXRD pattern (a) and BET surface area (b).

for 0, 10, 20 and 35 at% titanium samples. The broadening effects do not allow obtaining high accuracy on the cell parameters for the 35 at% Ti sample as it is the case for 10 and 20% samples. From the HRXPD diagrams, the cell parameters were refined using the whole powder pattern decomposition method (see the ESI and Fig. S6–S9†). A contraction of the *c* parameter was observed from 14.7290(5) to 14.5156(4) and 14.4558(3) Å going from MIL-173(Zr) to the MOF with 10 and 20 at% of titanium respectively, while it remains almost constant given the higher standard deviations for the 35 at% Ti. The [001] direction corresponds to the inorganic chain therefore the contraction of the *c* lattice parameter agrees with a gradual replacement of Zr(IV) by smaller Ti(IV) ions.

Periodic DFT calculations (see the ESI† for the computational details) were performed to model the incorporation and distribution of Ti ions within the framework. Simulations with Ti atomic content of 12.5%, 25%, 37.5% and 50% were run allowing the relaxation of the atomic positions and lattice parameters. In all cases, Ti atoms adopt the dodecahedral geometry, likewise the Zr atoms. This 8-fold coordination geometry, although rare for Ti, has been already observed in few crystal structures.[50–53] Furthermore, the reduction of the coordination number to a lower value (*e.g.* 6, as commonly observed with Ti(IV)) can be obtained exclusively through the rotation of gallate groups. This would lead to extremely distorted TiO_6 polyhedra, which are unlikely to be observed experimentally. In accordance with the experimental PXRD data, a shrinkage of the cell volume was found. In the simulations, cell volume reductions of 0.7%, 1.6%, 2.6% and 2.9% were calculated for the systems with Ti at% of 12.5, 25, 37.5 and 50% respectively. These values are in rather good agreement with the evolution of the cell parameters obtained from the full pattern matching of the experimental HRXRPD data (cell volume reduction of 1.5%, 1.7% and 2% for MIL-173(Zr/Ti)-10, -20 and -35, respectively, see Table S7†). Interestingly, analyzing the total energies of different configurations (see the ESI†), it was found that Ti ions tend to be located as far as possible from each other (Fig. 4 and Tables S1–S3†). This suggests that the inclusion of Ti into the framework produces some strains, explaining the reduction of crystallinity at high Ti at%. Even at a ratio of 50%, the most stable configuration is the one with alternating Ti and Zr atoms. These calculations suggest that a homogeneous dispersion of Ti inside the inorganic chains is more favored than segregated Ti and Zr nanodomains in the crystals.

The evolution of the porosity along the increasing Ti content was investigated by nitrogen sorption at 77 K. In all cases, type I sorption isotherms were obtained, attesting the microporous structure of all the compounds (Fig. S10†). For low Ti content, a slight increase in the BET surface area is observed (920 and 960 $m^2\ g^{-1}$ for MIL-173(Zr) and MIL-173(Zr/Ti)-5, respectively) which could be due to the lower molar mass of Ti compared to Zr. The surface area remains almost unaltered up to 30 at% Ti loading, indicating that the titanium incorporation process doesn't take place inside the pores but only in the inorganic chain of the MOF. Then, the BET SA decreases to 750 and 550 $m^2\ g^{-1}$ for 40 and 50 at% Ti loadings respectively (Fig. 3b and

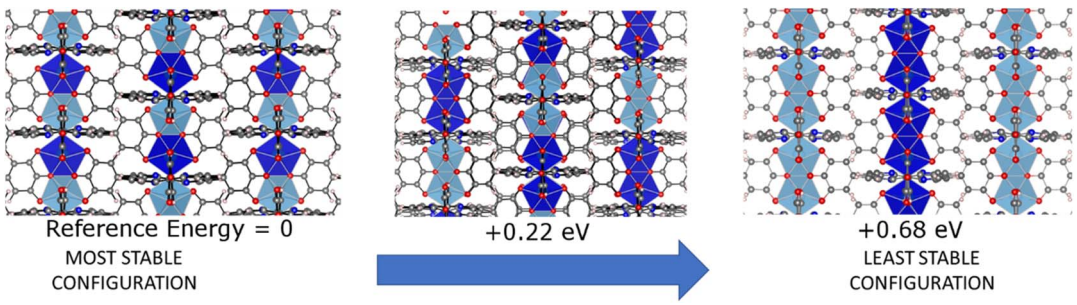

Fig. 4 Different configurations for simulated MIL-173(Zr/Ti)-50 (with 50 at% Ti in the structure). On the left the most stable configuration in which the Ti atoms are alternated by Zr atoms. On the right the least stable configuration in which all Ti atoms are close to each other. The total energy of the most stable configuration was used as the reference energy.

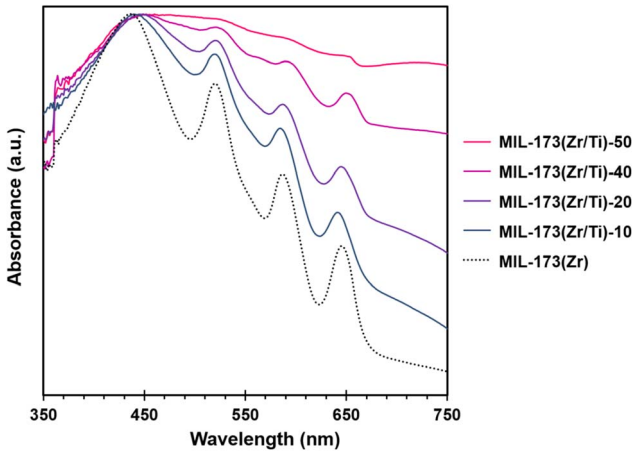

Fig. 5 UV-vis absorption spectra of the parent MIL-173(Zr) and the mixed-metal MIL-173(Ti/Zr) samples.

S10†). The porosity decrease is observed for samples with less ordered, therefore more defective structures as depicted in the SEM and PXRD data.

To get further insight, surface areas were evaluated by simulation (see the ESI† for details).[54,55] In line with the experimental results, simulations show that the internal surface area increases slightly (*ca.* +1%) for a low amount of Ti (12.5 at%), and it reduces when going to a higher amount (*ca.* −2% for 37.5 at% Ti). The decrease in the theoretical surface area is much smaller than the one observed experimentally, corroborating the idea that at high loading of Ti more defects are present, which are not tackled by the simulation.

Electronic microscopy, X-ray diffraction and sorption isotherm measurements all together point a gradual change of the sample with increasing Ti content, corroborating the fact that Ti is coordinated by the porphyrinic linker rather than deposited as an inorganic oxide on the Zr MOF surface. This observation is also supported by the simulations and is further backed up by the UV-visible spectroscopic analysis of MIL-173(Zr) and the mixed-metal samples. As shown in Fig. 5, the MIL-173(Zr) UV-vis absorption spectrum is characteristic of the absorption bands originating from the π–π* transitions of the free base porphyrin macrocycle, displaying a strong Soret absorption band at 440 nm, and three Q bands at 523, 588 and 643 nm. In the mixed metal samples, the above-mentioned bands remain clearly visible. Specifically, the presence of three Q bands with unchanged corresponding wavelengths shows that Ti ions are not coordinated by the pyrrolic functions of the porphyrinic macrocycle. This agrees with the very demanding conditions needed to access titanyl porphyrins.[56] More importantly, the signal is superimposed with a broad absorption feature indicative of the ligand-to-metal-charge-transfer (LCMCT) band characteristic of Ti–phenolate complexes,[57] unambiguously proving that Ti is present within the inorganic chain.

The frontier orbitals were then calculated, and the results match with the finding of the UV-vis analyses. MIL-173(Zr) presents a ligand centered π–π* transition, while, after the insertion of Ti, an additional transition appears from the ligand π to the empty Ti d orbitals (Fig. 6). This is due to the Ti 3d orbitals being closer in energy to the ligand O orbitals than Zr 4d, so they can overlap forming a crystalline orbital. The change in the lowest unoccupied crystal orbital (LUCO) has a direct consequence in the band gap, which decreases from 2.44 eV to 2.31 eV. Although the absolute values of band gaps calculated by hybrid DFT are not accurate, the trend is expected to be meaningful. This was confirmed experimentally by the X-ray Photoelectron Spectrometry (XPS) experiment, as described below.

XPS and energy level diagram

The most photocatalytically active MIL-173(Zr/Ti)-40 sample prepared in this study and its parent MIL-173(Zr) solid were also characterized by means of XPS (Fig. 7). XPS is a common technique employed for the characterization of the elements present in a MOF as well as their oxidation state.[58] This technique has also been employed in the field of metal oxides[59,60] as well as MOFs[15,58,61] to obtain experimental evidence about the presence of a mixture of cations in the same domain. In the present study, C 1s spectra show the presence of three main bands centered at 284.4, 285.8 and 288.5 eV characteristic of the C–C sp^2, C–N/C=N and C–O present in the porphyrin ligand. The O 1s spectra show two main bands at 531 and 533 eV that can be attributed to the phenolate ($C–O^-$) and phenolic (C–O–H) oxygen atoms, respectively. The deconvoluted N 1s spectra can be assigned to the presence of nitrogen atoms in the form of –NH– (399.4 eV) and –C=N– (397.4 eV) groups. Comparison of C 1s, O 1s and N 1s signals obtained for MIL-173(Zr) and MIL-173(Zr/Ti)-40 reveals that the environment of these elements in both solids resembles to a large extent. The Zr 3d spectra of both MOFs agree with the presence of Zr^{4+}. The lower Zr 3d intensity observed in the case of the MIL-173(Zr/Ti)-40 is in good agreement with its lower zirconium content (about 60 at%) with respect to the monometallic MIL-173(Zr). In addition, for MIL-173(Zr/Ti)-40, a small but significant shift (0.33 eV) of this signal towards lower binding energy with respect to the parent MIL-173(Zr) is detected. Previous studies using mixed zirconium and titanium oxides have associated such a shift with the presence of Zr–O–Ti chemical bonds.[59,60] In the field of MOFs, a similar shift (0.32 eV) towards lower binding energies was also observed for UiO-66(Zr/Ti) when compared to UiO-66(Zr).[15,61] Eventually, XPS analyses agree with previous characterizations on MIL-173(Zr/Ti), confirming the intimate mixture of Ti and Zr ions within the inorganic chains, rather than the presence of Zr-rich and Ti-rich nano-domains. In addition, the deconvoluted Ti 2p XPS obtained for the mixed-metal MIL-173(Zr/Ti)-40 can be assigned to the presence of Ti(IV) (Fig. S13e†).

One of the essential prerequisites for a solid to be employed as a heterogeneous photocatalyst is to have an energy level diagram in accordance with the thermodynamics of the process.[62] For this purpose, the energy level diagrams of MIL-173(Zr/Ti)-40 and the parent MIL-173(Zr) were determined. The Tauc plots, calculated from the solid-state UV-vis reflectance spectra (Fig. S15†), were employed to estimate the optical

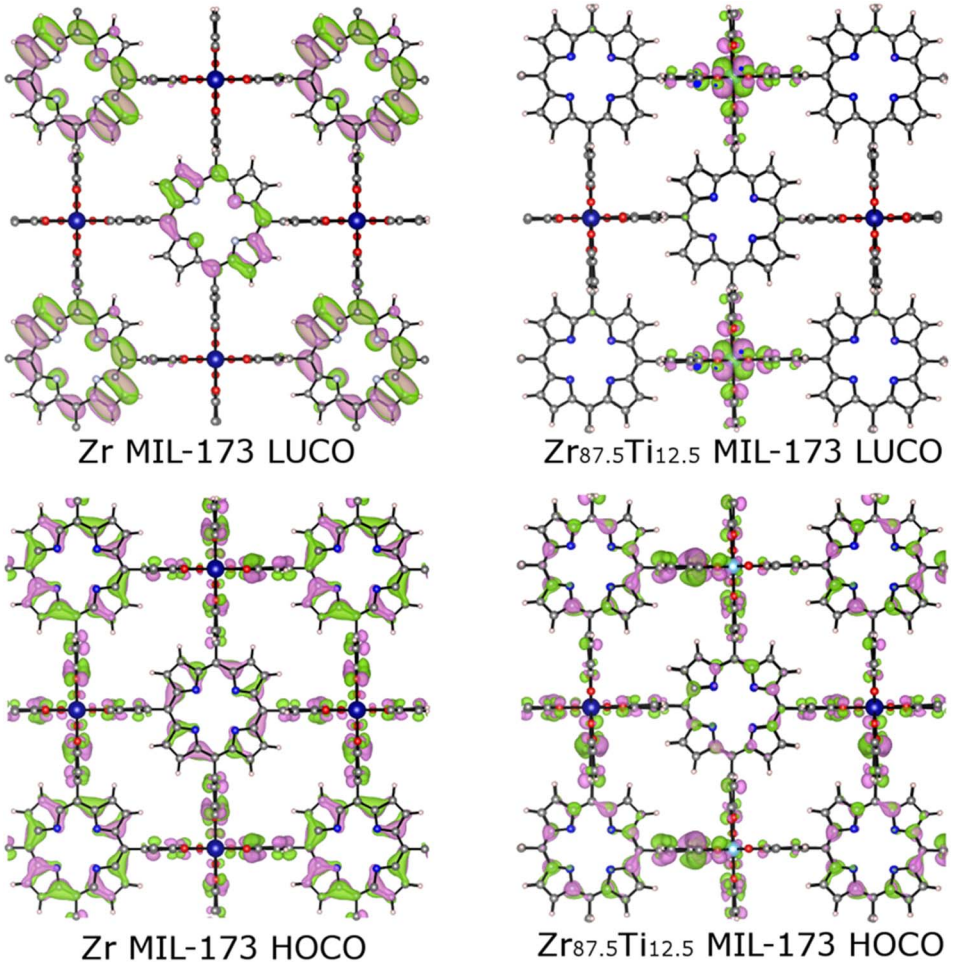

Fig. 6 HOCO and LUCO orbitals for the parent MIL-173(Zr) and the mixed metal MIL-173(Zr/Ti)-12.5. Atom colour scheme: big dark blue sphere = Zr; big cyan sphere = Ti; small grey sphere = C; small blue sphere = N; small red sphere = O; small pink sphere = H.

band gaps of both solids. Values of 1.83 and 1.88 eV were obtained for MIL-173(Zr/Ti)-40 and MIL-173(Zr), respectively (Fig. 8). XPS analysis was further used to estimate the level of the valence bands Evf, which is equal to 1.82 eV for both solids (Fig. S14a and b†). From these values and applying the equation $Ev^{NHE} = Ev^{f} + \phi_{sp} - 4.44$, where ϕ_{sp} is the work function of the spectrometer (equal to 4.244 eV), the energy of the HOCOs *versus* NHE was estimated. Eventually, the position of the LUCOs was obtained by adding to these values the optical band gap. Fig. 8 shows that the estimated energy level diagrams for MIL-173(Zr/Ti)-40 and MIL-173(Zr) are suitable for the solar-driven photocatalytic water splitting into H_2 and O_2. The somehow lower band gap value of MIL-173(Zr/Ti)-40 compared to MIL-173(Zr) is mainly attributed to the lowering of the LUCO due to the presence of titanium atoms as deduced from DFT calculations.

Photocatalytic activity

The series of MIL-173(Zr/Ti) solids with variable Ti at% and the parent MIL-173(Zr) were evaluated for the photocatalytic OWS under simulated sunlight irradiation. Solids were suspended in water (0.5 mg mL^{-1}) and submitted to simulated sunlight irradiation for 22 hours. Fig. 9 shows that both the monometallic MIL-173(Zr) and bimetallic MIL-173(Zr/Ti) solids photocatalytically split H_2O into H_2 and O_2. Interestingly, the photocatalytic activity increases with the amount of titanium content up to 40 at%. This enhancement of photocatalytic activity agrees with previous experimental and theoretical results which indicate that the presence of low-lying empty 3d orbitals of titanium atoms in the inorganic building unit favors the photoinduced LMCT pathway between the porphyrin ligand and the inorganic units of the MOF.[63–65] More specifically, DFT calculations have shown that the titanium ions contribute to the LUCO and decrease the required energy to promote the photoinduced ligand-to-metal charge transfer. As discussed later, additional experimental characterization of the MOFs by means of photocurrent measurements and photoluminescence spectroscopy further confirmed that Ti facilitates this reaction pathway.

Increasing further the titanium content to 50 at% results in a somehow lower photocatalytic activity (Fig. 9a). The results indicate that the photocatalytic activity of MIL-173(Zr/

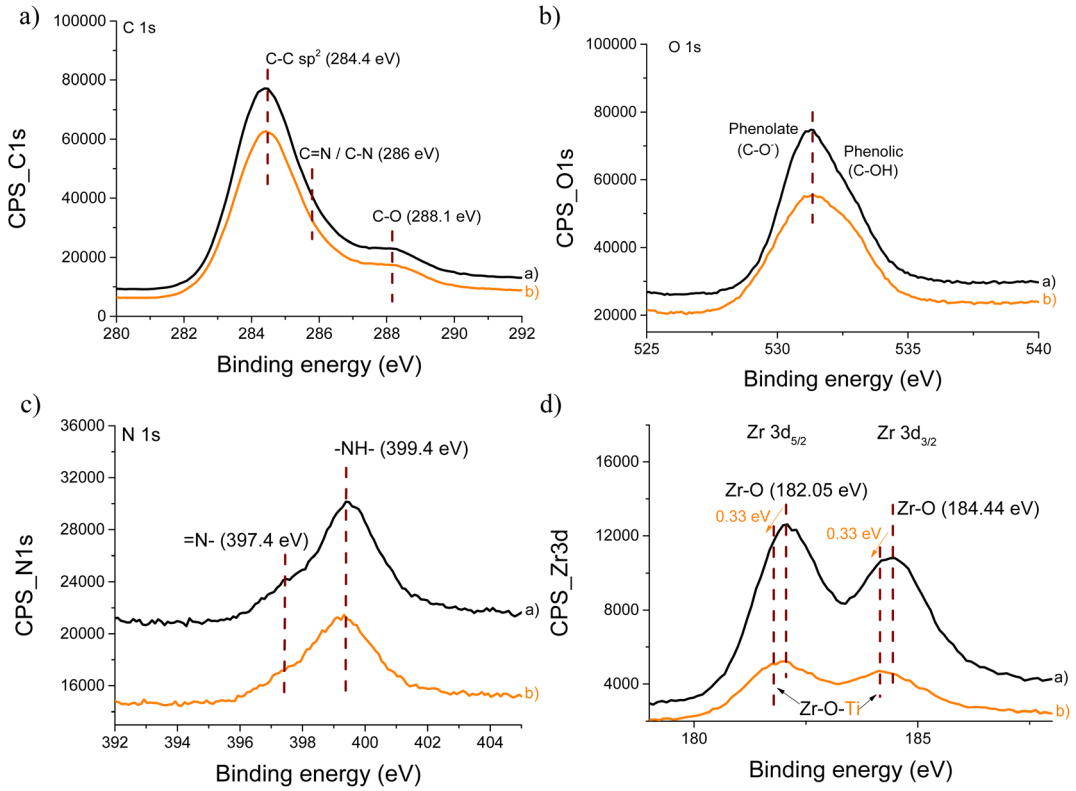

Fig. 7 XPS spectra comparison of C 1s (a), O 1s (b), N 1s (c) and Zr 3d (d) for the MIL-173(Zr) (black line) and MIL-173(Zr/Ti)-40 (orange line) samples.

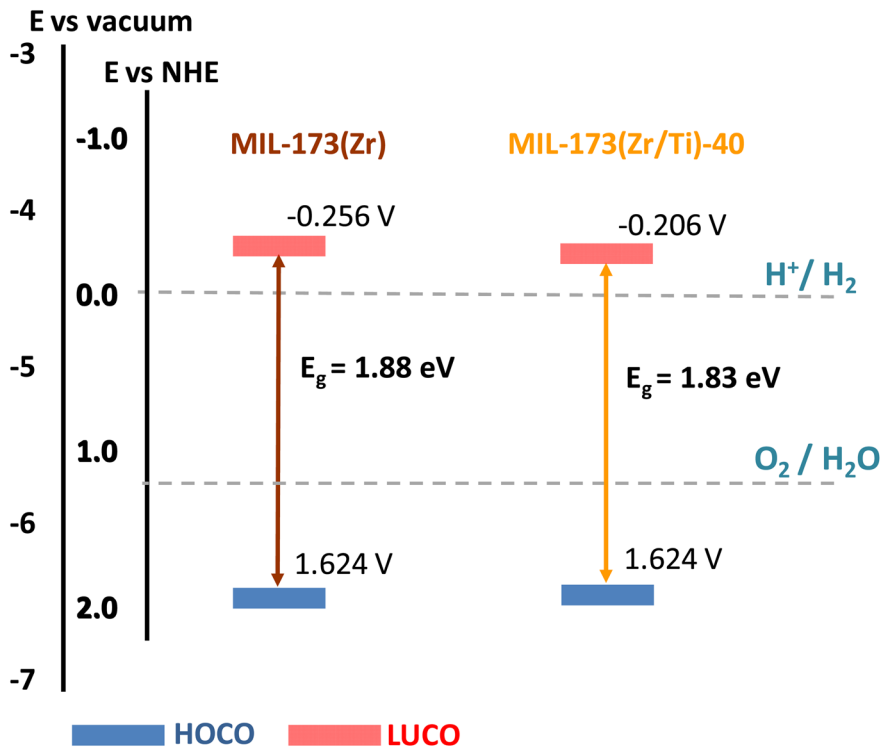

Fig. 8 Energy level diagrams for MIL-173(Zr) and MIL-173(Zr/Ti)-40 samples.

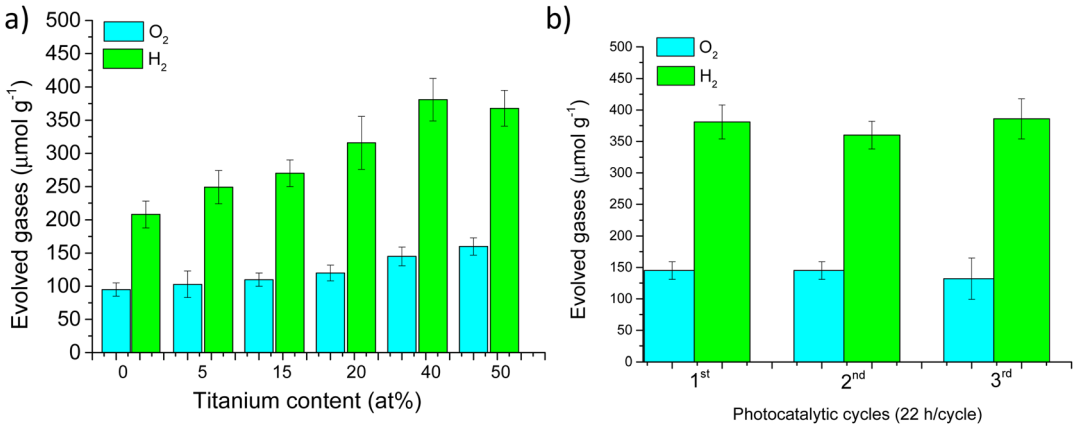

Fig. 9 (a) Photocatalytic OWS under simulated sunlight irradiation using MIL-173(Zr) and MIL-173(Zr/Ti) solids having different Ti at% contents; (b) evaluation of the reusability of the MIL-173(Ti/Zr)-40 photocatalyst for OWS (3 cycles). Experimental conditions: MIL-173(Zr/Ti) (10 mg), H_2O (20 mL), simulated sunlight irradiation (Hg–Xe lamp together with an AM 1.5 G filter), reaction time (22 h).

Table 1 Photocatalytic activity achieved with MOFs for the overall water splitting under visible or simulated sunlight irradiation

Catalyst	Co-catalyst	Reaction conditions	Photocatalytic activity	Reference
MIL-173(Zr/Ti)-40	—	Photocatalyst (10 mg), H_2O (20 mL), simulated sunlight irradiation (Xe–Hg lamp 150 W, 1.5 AM filter), 35 °C, 22 h	381 and 145 μmol g^{-1} for H_2 and O_2, respectively	This work
MIL-173(Zr/Ti)-40	—	Photocatalyst (10 mg), H_2O (20 mL), visible light irradiation (>420 nm; Xe–Hg lamp 150 W, GG420 filter), 35 °C, 22 h	186 and 79 μmol g^{-1} for H_2 and O_2, respectively	This work
MIL-173(Zr/Ti)-40	—	Photocatalyst (10 mg), H_2O (20 mL), visible light irradiation (>495 nm; Xe–Hg lamp 150 W, GG495 filter), 35 °C, 22 h	131 and 54 μmol g^{-1} for H_2 and O_2, respectively	This work
IEF-11	—	Photocatalyst (10 mg), H_2O (20 mL), simulated sunlight irradiation (Xe–Hg lamp 150 W, 1.5 AM filter), 35 °C, 22 h	260 and 107 μmol g^{-1} for H_2 and O_2, respectively	20
Plasma-treated MIL-125(Ti)–NH_2	—	Photocatalyst (20 mg), H_2O (20 mL), 35 °C, solar simulator (1 sun), 22 h	~83 and 29 μmol g^{-1} for H_2 and O_2, respectively	19
UiO-66(Zr/Ce/Ti)	—	Photocatalyst (20 mg), H_2O (20 mL), visible light irradiation (Hg–Xe lamp 150 W with a l > 450 nm cut-off filter)	210 and 70 μmol g^{-1} for H_2 and O_2, respectively	15
MIL-125(Ti)–NH_2	Pt and RuO_x	Photocatalyst (20 mg/20 mL Milli Q-H_2O), natural sunlight (100 mW × cm^{-2}), ambient temperature 30 °C, 10 h	27 and 14 μmol g^{-1} for H_2 and O_2, respectively	18
Liposome-based MOF	Pt–porphyrin and Ir–bipyridine	Photocatalyst suspension, redox relays (tetrachlorobenzoquinone/tetrachlorobenzohydrosemiquinone), and (Fe^{3+}/Fe^{2+}), H_2O (20 mL), 72 h, light source 400 nm LED + 450 nm LED836 and 418 μmol g^{-1} for H_2 and O_2, respectively22		

Ti) increases along the titanium content up to 40 at% and, then, a plateau is observed. As mentioned earlier, MIL-173(Zr/Ti)-50 exhibits a significantly reduced surface area, suggesting that a high porosity is required to achieve the highest catalytic activity, as found in MIL-173(Zr/Ti)-40.

The reusability of the MOF presenting the optimal composition was further evaluated. Fig. 9b shows that the MIL-173(Zr/Ti)-40 can be reused at least three times without any decrease of the photocatalytic activity. As shown in Fig. S18,† after these three cycles, the solid remains crystalline. Moreover, SEM/EDS analysis shows that the MOF morphology as well as the Ti/Zr ratio remains unchanged (Fig. S17, Table S10†). Eventually, ICP-OES analysis of the aqueous solution (after the removal of MIL-173(Zr/Ti)-40 by filtration) allows estimating the level of leaching. Even after three cycles, only a negligible amount of cations were found in solution (<0.1 and <0.3 wt% for Zr and Ti, respectively). This confirms that the solid is stable under the working conditions, and that the photocatalytic process is heterogeneous.

The performance of MIL-173(Zr/Ti)-40 for OWS was compared with the reported values of other MOFs (Table 1). It can be seen that this solid even without any co-catalyst ranks among the most active MOFs reported so far. It is also remarkable the good photocatalytic activity is achieved using MIL-173(Zr/Ti)-40 under exclusively visible light irradiation at wavelengths higher than 420 or 495 nm. These observations can be associated with the adequate energy level diagram of MIL-173(Zr/Ti)-40 for the OWS (Fig. 8). The estimated apparent quantum yield (AQY) for the photocatalytic OWS using MIL-173(Zr/Ti)-40 is equal to 0.11% at 450 nm. For comparison a complex liposome-based MOF (Table 1) constituted by an integrated HER counterpart having a Zn–porphyrin as the light harvester and Pt–porphyrin as catalytic centers together with an oxygen evolution reaction counterpart having a [Ru(2,2′-bipyridine)$_3$]$^{2+}$ complex as the photosensitizer and Ir–bipyridine as catalytic centres combined with the use of two redox relays [tetrachlorobenzoquinone/tetrachlorobenzohydrosemiquinone and (Fe^{3+}/Fe^{2+})] achieved an AQY for the OWS of 1.5 ± 1% at 436 nm.[22]

Reaction mechanism

For the most active MIL-173(Zr/Ti)-40 sample, an additional photocatalytic test was performed in isotopically labeled $H_2{}^{18}O$. The observation of the formation of $^{18}O_2$ by mass spectrometry (m/z 36) allows us to unambiguously confirm that oxygen is formed from the oxidation of water (Fig. S16†).

To gain additional information about the occurrence of photoinduced charge separation in the MIL-173(Zr) and MIL-

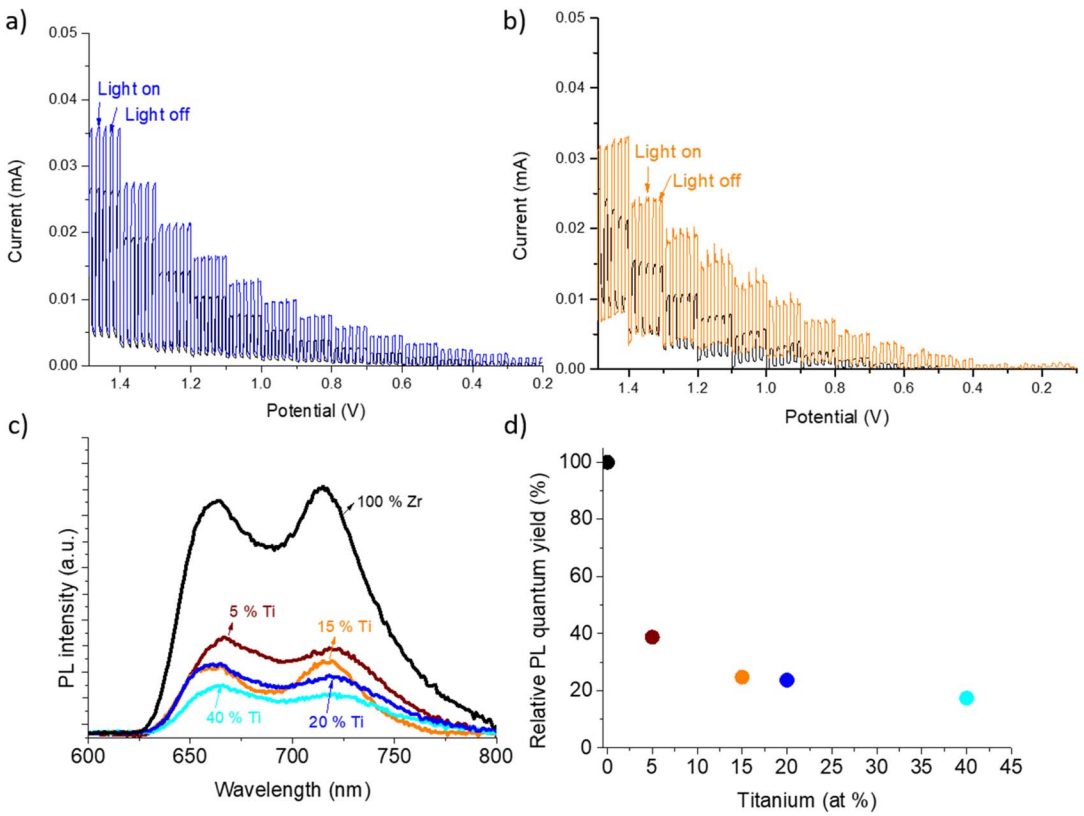

Fig. 10 Current intensity *versus* polarization potential measured for MIL-173(Zr/Ti)-40 (a) and MIL-173(Zr) (b). Samples supported on an FTO electrode in an air-free acetonitrile solution ((TBA)PF_6, 0.1 M) in the absence (black lines) or in the presence of methanol (blue and orange lines) upon UV-vis irradiation. Photoluminescence (PL) spectra measured for the MIL-173 samples having different Zr/Ti at ratios upon excitation at 440 nm (c). Relative PL quantum yield of the MIL-173(Zr/Ti) samples with respect to the parent MIL-173(Zr) from the spectra of panel (c) (d).

173(Zr/Ti)-40 samples, photocurrent measurements were performed.[19,66] For this purpose, thin films of MIL-173(Zr) or MIL-173(Zr/Ti)-40 were deposited on a transparent conductive electrode of FTO and used as working electrodes. Fig. 10 shows the measured current under both dark and UV-vis irradiation of these two electrodes at increasing positive voltages. These results indicate that the MIL-173(Zr/Ti)-40 sample deposited on FTO exhibits higher photocurrent than the parent MIL-173(Zr)/FTO measured in a solution of $(TBA)PF_6$ (TBA = tetra-*n*-butylammonium) dissolved in acetonitrile. The addition of methanol during these photocurrent experiments using either MIL-173(Zr)/FTO or MIL-173(Zr/Ti)-40/FTO leads to an increase of the photocurrent. These observations agree with the role of methanol as an electron donor that quenches the photogenerated holes in the MIL-173 samples under UV-vis irradiation, decreasing the possibility of electron–hole recombination and, therefore, leading to an increase of photogenerated electrons responsible for the observed photocurrent. Interestingly, the increase of photocurrent intensity is higher when using the MIL-173(Zr/Ti) samples instead of the parent MIL-173(Zr). These data confirm the positive role of the presence of titanium in the mixed-metal MIL-173(Zr/Ti) acting as an electron acceptor of photogenerated electrons. All these photocurrent observations correlate well with the higher photocatalytic activity during the overall water splitting under simulated sunlight irradiation using the mixed-metal MIL-173(Zr/Ti)-40 than the monometallic MIL-173(Zr).

To further study the influence of the presence of titanium atoms in MIL-173(Zr/Ti), photoluminescence (PL) measurements were carried out. PL spectroscopy is commonly employed to evaluate the relative efficiency of the photoinduced charge separation in MOFs.[67] For this purpose, acetonitrile suspensions of MOFs were prepared and their absorbance at 440 nm was adjusted to 0.4. The absorption band at 440 nm corresponds to the porphyrin Soret band. As shown on Fig. 10c, upon photoexcitation at 440 nm, the suspensions of MIL-173(Zr/Ti) present two maximum emission bands at about 660 and 715 nm. Interestingly, increasing the Ti atomic content in MIL-173(Zr/Ti) results in the gradual decrease of the emission intensity. Fig. 10d shows the evolution of the relative PL quantum yield of MIL-173(Zr/Ti) samples with respect to the parent MIL-173(Zr) solid. This result can be understood considering that titanium present in the metal nodes of MIL-173(Zr/Ti) favors the photoinduced charge separation. These data confirm the positive effect of the presence of titanium in the MIL-173(Zr/Ti) samples for the photocatalytic process (Fig. 9a).

In summary, the photocurrent and photoluminescence experiments indicate that the bimetallic MIL-173(Zr/Ti) exhibits a more efficient photoinduced charge separation with respect to the parent MIL-173(Zr), in line with the higher photocatalytic activity for the OWS.

Conclusions

The present study shows the possibility of developing a mixed-metal Zr/Ti–porphyrin MIL-173 material with exceptional photocatalytic activity for the OWS into H_2 and O_2 under simulated sunlight irradiation. The high activity of the optimized MIL-173(Zr/Ti)-40 can be attributed to several factors such as its appropriate energy level diagram for the OWS under sunlight irradiation that can operate under a photoinduced ligand-to-metal charge transfer mechanism as revealed by DFT calculations, photoluminescence spectroscopy together with photocurrent measurements. Considering the large tunability and flexibility of MOFs we consider that this study will contribute to the development of efficient MOF-based materials for the solar-driven OWS.

Conflicts of interest

There are no conflicts to declare.

Acknowledgements

The authors would like to thank the French National Research Agency for the JCJC STREAM research grant (ANR-17-CE09-0029-01). Grant PID2021-123856OB-I00 was funded by MCIN/AEI/10.13039/501100011033 and by "ERDF A way of making Europe", by the "European Union". Grant FPU20/03140 was funded by MCIN/AEI/10.13039/501100011033 and, as appropriate, by "ESF Investing in your future" or by "European Union NextGenerationEU/PRTR". The French Ministry of Higher Education and Research is acknowledged for the studentship of B. G. and the Centre Technologique des Microstructures of Lyon University for providing electronic microscopy facilities.

References

1 Y.-B. Huang, J. Liang, X.-S. Wang and R. Cao, *Chem. Soc. Rev.*, 2017, **46**, 126–157.
2 J.-W. Yoon, J.-H. Kim, C. Kim, H. W. Jang and J.-H. Lee, *Adv. Energy Mater.*, 2021, **11**, 2003052.
3 A. Dhakshinamoorthy, A. M. Asiri and H. García, *Angew. Chem., Int. Ed.*, 2016, **55**, 5414–5445.
4 M. B. Majewski, A. W. Peters, M. R. Wasielewski, J. T. Hupp and O. K. Farha, *ACS Energy Lett.*, 2018, **3**, 598–611.
5 C. Gomes Silva, I. Luz, F. X. Llabrés i Xamena, A. Corma and H. García, *Chem.–Eur. J.*, 2010, **16**, 11133–11138.
6 R. Jaryal, R. Kumar and S. Khullar, *Coord. Chem. Rev.*, 2022, **464**, 214542.
7 D. A. Reddy, Y. Kim, M. Gopannagari, D. P. Kumar and T. K. Kim, *Sustainable Energy Fuels*, 2021, **5**, 1597–1618.
8 Y.-N. Gong, J.-H. Mei, J.-W. Liu, H.-H. Huang, J.-H. Zhang, X. Li, D.-C. Zhong and T.-B. Lu, *Appl. Catal., B*, 2021, **292**, 120156.
9 J.-W. Wang, K. Yamauchi, H.-H. Huang, J.-K. Sun, Z.-M. Luo, D.-C. Zhong, T.-B. Lu and K. Sakai, *Angew. Chem., Int. Ed.*, 2019, **58**, 10923–10927.
10 H. L. Nguyen, *Adv. Mater.*, 2022, **34**, 2200465.
11 H. L. Nguyen, *Sol. RRL*, 2021, **5**, 2100198.
12 Y. An, Y. Liu, P. An, J. Dong, B. Xu, Y. Dai, X. Qin, X. Zhang, M.-H. Whangbo and B. Huang, *Angew. Chem., Int. Ed.*, 2017, **56**, 3036–3040.

13 X.-P. Wu, L. Gagliardi and D. G. Truhlar, *J. Am. Chem. Soc.*, 2018, **140**, 7904–7912.
14 X.-P. Wu, L. Gagliardi and D. G. Truhlar, *J. Chem. Phys.*, 2019, **150**, 041701.
15 A. Melillo, M. Cabrero-Antonino, S. Navalón, M. Álvaro, B. Ferrer and H. García, *Appl. Catal., B*, 2020, **278**, 119345.
16 J. Zhang, T. Bai, H. Huang, M.-H. Yu, X. Fan, Z. Chang and X.-H. Bu, *Adv. Mater.*, 2020, **32**, 2004747.
17 Y. An, B. Xu, Y. Liu, Z. Wang, P. Wang, Y. Dai, X. Qin, X. Zhang and B. Huang, *ChemistryOpen*, 2017, **6**, 701–705.
18 S. Remiro-Buenamañana, M. Cabrero-Antonino, M. Martínez-Guanter, M. Álvaro, S. Navalón and H. García, *Appl. Catal., B*, 2019, **254**, 677–684.
19 M. Cabrero-Antonino, J. Albero, C. García-Vallés, M. Álvaro, S. Navalón and H. García, *Chem.–Eur. J.*, 2020, **26**, 15682–15689.
20 P. Salcedo-Abraira, A. A. Babaryk, E. Montero-Lanzuela, O. R. Contreras-Almengor, M. Cabrero-Antonino, E. S. Grape, T. Willhammar, S. Navalón, E. Elkäim, H. García and P. Horcajada, *Adv. Mater.*, 2021, **33**, 2106627.
21 P. Salcedo-Abraira, S. M. F. Vilela, A. A. Babaryk, M. Cabrero-Antonino, P. Gregorio, F. Salles, S. Navalón, H. García and P. Horcajada, *Nano Res.*, 2021, **14**, 450–457.
22 H. Hu, Z. Wang, L. Cao, L. Zeng, C. Zhang, W. Lin and C. Wang, *Nat. Chem.*, 2021, **13**, 358–366.
23 Y. Fu, D. Sun, Y. Chen, R. Huang, Z. Ding, X. Fu and Z. Li, *Angew. Chem., Int. Ed.*, 2012, **51**, 3364–3367.
24 T. Devic and C. Serre, *Chem. Soc. Rev.*, 2014, **43**, 6097–6115.
25 J. Zhu, P.-Z. Li, W. Guo, Y. Zhao and R. Zou, *Coord. Chem. Rev.*, 2018, **359**, 80–101.
26 H. Assi, G. Mouchaham, N. Steunou, T. Devic and C. Serre, *Chem. Soc. Rev.*, 2017, **46**, 3431–3452.
27 Y. Horiuchi, T. Toyao, M. Saito, K. Mochizuki, M. Iwata, H. Higashimura, M. Anpo and M. Matsuoka, *J. Phys. Chem. C*, 2012, **116**, 20848–20853.
28 C. H. Hendon, D. Tiana, M. Fontecave, C. Sanchez, L. D'arras, C. Sassoye, L. Rozes, C. Mellot-Draznieks and A. Walsh, *J. Am. Chem. Soc.*, 2013, **135**, 10942–10945.
29 L. Zou, R. Sa, H. Lv, H. Zhong and R. Wang, *CHEMSUSCHEM*, 2020, **13**, 6124–6140.
30 P. D. Harvey, *J. Mater. Chem. C*, 2021, **9**, 16885–16910.
31 X. Zhang, M. C. Wasson, M. Shayan, E. K. Berdichevsky, J. Ricardo-Noordberg, Z. Singh, E. K. Papazyan, A. J. Castro, P. Marino, Z. Ajoyan, Z. Chen, T. Islamoglu, A. J. Howarth, Y. Liu, M. B. Majewski, M. J. Katz, J. E. Mondloch and O. K. Farha, *Coord. Chem. Rev.*, 2021, **429**, 213615.
32 S. Yuan, T.-F. Liu, D. Feng, J. Tian, K. Wang, J. Qin, Q. Zhang, Y.-P. Chen, M. Bosch, L. Zou, S. J. Teat, S. J. Dalgarno and H.-C. Zhou, *Chem. Sci.*, 2015, **6**, 3926–3930.
33 Y. Keum, S. Park, Y.-P. Chen and J. Park, *Angew. Chem., Int. Ed.*, 2018, **57**, 14852–14856.
34 M. Kim, J. F. Cahill, H. Fei, K. A. Prather and S. M. Cohen, *J. Am. Chem. Soc.*, 2012, **134**, 18082–18088.
35 A. Wang, Y. Zhou, Z. Wang, M. Chen, L. Sun and X. Liu, *RSC Adv.*, 2016, **6**, 3671–3679.
36 J. Tu, X. Zeng, F. Xu, X. Wu, Y. Tian, X. Hou and Z. Long, *Chem. Commun.*, 2017, **53**, 3361–3364.
37 G. Ye, H. Qi, X. Li, K. Leng, Y. Sun and W. Xu, *ChemPhysChem*, 2017, **18**, 1903–1908.
38 Y. Lee, S. Kim, J. K. Kang and S. M. Cohen, *Chem. Commun.*, 2015, **51**, 5735–5738.
39 X. Chen, Y. Kuwahara, K. Mori, C. Louis and H. Yamashita, *J. Mater. Chem. A*, 2020, **8**, 1904–1910.
40 Y. Feng, Q. Chen, M. Cao, N. Ling and J. Yao, *ACS Appl. Nano Mater.*, 2019, **2**, 5973–5980.
41 J. Tan, X. He, F. Yin, X. Liang and G. Li, *Int. J. Hydrogen Energy*, 2021, **46**, 31647–31658.
42 M. S. Denny, L. R. Parent, J. P. Patterson, S. K. Meena, H. Pham, P. Abellan, Q. M. Ramasse, F. Paesani, N. C. Gianneschi and S. M. Cohen, *J. Am. Chem. Soc.*, 2018, **140**, 1348–1357.
43 Y. Han, M. Liu, K. Li, Q. Sun, W. Zhang, C. Song, G. Zhang, Z. C. Zhang and X. Guo, *Inorg. Chem. Front.*, 2017, **4**, 1870–1880.
44 F. Nouar, T. Devic, H. Chevreau, N. Guillou, E. Gibson, G. Clet, M. Daturi, A. Vimont, J. M. Grenèche, M. I. Breeze, R. I. Walton, P. L. Llewellyn and C. Serre, *Chem. Commun.*, 2012, **48**, 10237–10239.
45 G. Mouchaham, B. Abeykoon, M. Giménez-Marqués, S. Navalon, A. Santiago-Portillo, M. Affram, N. Guillou, C. Martineau, H. Garcia, A. Fateeva and T. Devic, *Chem. Commun.*, 2017, **53**, 7661–7664.
46 L. Cooper, N. Guillou, C. Martineau, E. Elkaim, F. Taulelle, C. Serre and T. Devic, *Eur. J. Inorg. Chem.*, 2014, **2014**, 6281–6289.
47 Md. A. Rahim, M. Björnmalm, T. Suma, M. Faria, Y. Ju, K. Kempe, M. Müllner, H. Ejima, A. D. Stickland and F. Caruso, *Angew. Chem., Int. Ed.*, 2016, **55**, 13803–13807.
48 S. De, G. C. Quan, B. Gikonyo, C. Martineau-Corcos, C. Bousige, L. Veyre, T. Devic, C. Marichy and A. Fateeva, *Inorg. Chem.*, 2020, **59**, 10129–10137.
49 H. Möckel, M. Giersig and F. Willig, *J. Mater. Chem.*, 1999, **9**, 3051–3056.
50 D. B. Dell'Amico, F. Calderazzo, S. Ianelli, L. Labella, F. Marchetti and G. Pelizzi, *J. Chem. Soc., Dalton Trans.*, 2000, 4339–4342.
51 Q. Zhang, H.-D. Lai and Q. Lin, *J. Solid State Chem.*, 2021, **297**, 122056.
52 C. Forte, M. Hayatifar, G. Pampaloni, A. M. R. Galletti, F. Renili and S. Zacchini, *J. Polym. Sci., Part A: Polym. Chem.*, 2011, **49**, 3338–3345.
53 N. A. Straessler, M. T. Caudle and T. L. Groy, *Acta Crystallogr., Sect. E: Struct. Rep. Online*, 2008, **64**, m48.
54 D. Ongari, P. G. Boyd, S. Barthel, M. Witman, M. Haranczyk and B. Smit, *Langmuir*, 2017, **33**, 14529–14538.
55 T. F. Willems, C. H. Rycroft, M. Kazi, J. C. Meza and M. Haranczyk, *Microporous Mesoporous Mater.*, 2012, **149**, 134–141.
56 P. Fournari, R. Guilard, M. Fontesse, J.-M. Latour and J.-C. Marchon, *J. Organomet. Chem.*, 1976, **110**, 205–217.
57 I. A. Janković, Z. V. Šaponjić, E. S. Džunuzović and J. M. Nedeljković, *Nanoscale Res. Lett.*, 2009, **5**, 81.

58 Q. Liu, H. Cong and H. Deng, *J. Am. Chem. Soc.*, 2016, **138**, 13822–13825.
59 M. Li, X. Li, G. Jiang and G. He, *Ceram. Int.*, 2015, **41**, 5749–5757.
60 C. Sun, L. Liu, L. Qi, H. Li, H. Zhang, C. Li, F. Gao and L. Dong, *J. Colloid Interface Sci.*, 2011, **364**, 288–297.
61 A. Santiago-Portillo, S. Navalón, M. Álvaro and H. García, *J. Catal.*, 2018, **365**, 450–463.
62 Q. Wang and K. Domen, *Chem. Rev.*, 2020, **120**, 919–985.
63 P. Parnicka, W. Lisowski, T. Klimczuk, A. Mikolajczyk and A. Zaleska-Medynska, *Appl. Catal., B*, 2022, **310**, 121349.
64 D. Sun, W. Liu, M. Qiu, Y. Zhang and Z. Li, *Chem. Commun.*, 2015, **51**, 2056–2059.
65 A. Santiago Portillo, H. G. Baldoví, M. T. García Fernandez, S. Navalón, P. Atienzar, B. Ferrer, M. Alvaro, H. Garcia and Z. Li, *J. Phys. Chem. C*, 2017, **121**, 7015–7024.
66 C. Xu, H. Liu, D. Li, J.-H. Su and H.-L. Jiang, *Chem. Sci.*, 2018, **9**, 3152–3158.
67 Y. Zhao, J. Wang, W. Zhu, L. Liu and R. Pei, *Nanoscale*, 2021, **13**, 4505–4511.